Shaping the Atomic-Scale Geometries of Electrodes to Control Optical and Electrical Performance of Molecular Devices

Zhikai Zhao, Ran Liu, Dirk Mayer, Maristella Coppola, Lu Sun, Youngsang Kim, Chuankui Wang, Lifa Ni, Xing Chen, Maoning Wang, Zongliang Li,* Takhee Lee,* and Dong Xiang*

A straightforward method to generate both atomic-scale sharp and atomic-scale planar electrodes is reported. The atomic-scale sharp electrodes are generated by precisely stretching a suspended nanowire, while the atomic-scale planar electrodes are obtained via mechanically controllable interelectrodes compression followed by a thermal-driven atom migration process. Notably, the gap size between the electrodes can be precisely controlled at subangstrom accuracy with this method. These two types of electrodes are subsequently employed to investigate the properties of single molecular junctions. It is found, for the first time, that the conductance of the amine-linked molecular junctions can be enhanced ≈50% as the atomic-scale sharp electrodes are used. However, the atomic-scale planar electrodes show great advantages to enhance the sensitivity of Raman scattering upon the variation of nanogap size. The underlying mechanisms for these two interesting observations are clarified with the help of density functional theory calculation and finite-element method simulation. These findings not only provide a strategy to control the electron transport through the molecule junction, but also pave a way to modulate the optical response as well as to improve the stability of single molecular devices via the rational design of electrodes geometries.

1. Introduction

Molecular electronic devices that utilize single molecules or molecular monolayers as active electronic components represent a promising approach to the ongoing miniaturization and integration of electronic devices. Although molecular-based electronics may not replace most of the silicon-based electronics in the near future, there are convincing reasons to believe that molecular electronic devices can complement silicon-based devices by providing new functionalities and enabling ultimate scaling to be reached. The goal of utilizing molecules as functional units in electronic circuits has motivated numerous researchers for years.[1–4] During the last decade, several methodologies with unique advantages have been proposed to obtain molecular junctions and to reveal the intrinsic properties of molecules.[5–17] In particular, scanning tunneling microscopy shows strong ability to form different types of molecular junctions (tip and substrate can be different materials), which makes it possible to realize new type of functional devices and to observe novel phenomenon.[18–21] Meanwhile, the effects of molecular anchors,[22–25] electrode material,[7,8] and external environment on the properties of single-molecule junctions have been investigated,[25–28] which is a large step toward the construction of functional molecular electronic devices. Nonetheless, a number of challenges still need to be overcome before single-molecule devices can be widely used as commercial products.

Z. Zhao, Dr. L. Sun, L. Ni, M. Wang, Prof. D. Xiang
Key Laboratory of Optical Information Science and Technology
Institute of Modern Optics
College of Electronic Information and Optical Engineering
Nankai University
Nankai 300071, China
E-mail: xiangdongde@126.com

R. Liu, Prof. C. Wang, Prof. Z. Li
School of Physics and Electronics
Shandong Normal University
Jinan 250014, China
E-mail: lizongliang@sdnu.edu.cn

Dr. D. Mayer, M. Coppola
Peter-Grünberg-Institute PGI-8
Bioelectronic Research Center Jülich GmbH and JARA
Fundamentals of Future Information Technology
Jülich 52425, Germany

Dr. Y. Kim
Chemical Sciences Division
Lawrence Berkeley National Laboratory
Berkeley, CA 94720, USA

Dr. X. Chen
Penn State Department of Chemistry
The Pennsylvania State University
104 Chemistry Building, University Park, PA 16802, USA

Prof. T. Lee
Department of Physics and Astronomy
Seoul National University
Seoul 08826, Korea
E-mail: tlee@snu.ac.kr

**ADVANCED
SCIENCE NEWS**
www.advancedsciencenews.com

NANO · MICRO
small
www.small-journal.com

As we know, the electrical performance of single molecular device is very easy to be influenced by the external environment conditions, especially strongly affected by nanoscale configuration of the molecule–electrode interface due to its extremely small dimension, which may seriously hinder the application of molecular devices.[14,28,29] Thus, it is critical to clarify the effect of electrodes geometry (extended to the atomic-scale level) on the performance of single molecular junctions. However, it is still a great challenge to address this issue due to the technical limitation of fabrication and characterization. Another challenge is that the conductance of the electronic device with single-molecule component is poor compared to silicon-based electronic devices.[2] To be widely used in the market, it is expected that molecular devices should be operated under low bias with minimum energy consumption. Therefore, it is essential to find a way to improve the conductance of single molecular devices for commercial applications. It will be wonderful if we can improve the conductance of single molecular device just by the controlling of the electrode geometries without changing the target molecules and electrode materials.

To elucidate the role of the atomic-scale geometry of electrodes in determining the conductance of molecular devices and to find the optimized atomic-scale geometries to improve the conductance of the molecular devices, we fabricated both atomic-scale sharp (cone-shaped) electrodes and atomic-scale planar (plane-shaped) electrodes employing mechanically controllable break junction (MCBJ) technique.[30–41] We observed that the signal-to-noise ratio can be greatly improved with cone-shaped electrodes, and we further observed that the conductance of the molecular junction with cone-shaped electrodes can be 50% higher than the one with plane-shaped electrodes. With the help of density functional theory (DFT) calculation, the underlying mechanism for the conductance modulation was revealed. Our results will assist in fabricating electrodes with regular and uniform geometries at atomic-scale and will help us improving the stability of the molecular devices at single-molecule level.

2. Electrodes' Fabrication

We employ a novel home-made MCBJ device to generate two types of electrodes. The design and working principle of the MCBJ device is depicted in **Figure 1** (detailed information can be found in Figure S1 in the Supporting Information). In brief, a metal bridge was prefabricated on the substrate. The bending force exerted to the substrate by the push rod will lead to elongation of the metal bridge. The ultimate break of the metal bridge will result in the formation of two separated microelectrodes. Notably, we employed a differential screw to indirectly control the movement of push rod (Figure 1a). The tiny difference between the pitches of two screw threads leads to a very small relative displacement between the push rod and counterposts (see Figure S2 in the Supporting Information). Thus, the stretching rate of metal bridge can be significantly slowed down. After the break of metal bridge, the two electrodes will separate (ΔX) upon a further displacement of the push rod (ΔZ). The attenuation factor, given by $r = \Delta X / \Delta Z$, is $\approx 6.3 \times 10^{-7}$ with our designed equipment (representing the smallest attenuation factor reported to date), which indicates that we can precisely control the gap size between electrodes with subangstrom accuracy (see Figure S8 in the Supporting Information).

Two types of electrodes were fabricated: one is an atomic-scale sharp electrode fabricated by mechanically one-way stretching a gold nanowire (Figure 1b–e) and the other is an atomic-scale planar electrode fabricated by several repeated stretch–recompress processes applied on a microwire. For the fabrication of atomic-scale sharp electrodes, a suspended nanowire with a double-cone-shaped constriction was prefabricated on the substrate as we previously reported.[42,43] Notably, to obtain a pair of electrodes with atomic-scale sharp tips, (1) we employed electron beam lithography to create the nanoscale bridge, i.e., the diameter of constriction can be reduced to ≈ 30 nm, which facilitates the elongation of the metal bridge during the stretch process; (2) we prehardened the polyimide insulation layer under high vacuum to prevent any unexpected deformation and to suppress the drift of the nanogap size; and (3) we use a low stretching rate (0.1 nm s^{-1}) to stretch the metal bridge; in this way, a pair of atomic-scale sharp electrodes, even metal atom chain, can be automatically generated.

For the fabrication of the atomic-scale planar electrodes, a commercially available gold wire with a 50 µm diameter was employed, and a notch around the wire was made manually with a scalpel blade (**Figure 2**a). Then, the gold wire was fixed at two points by epoxy-glue to suspend the notch. The notch was broken
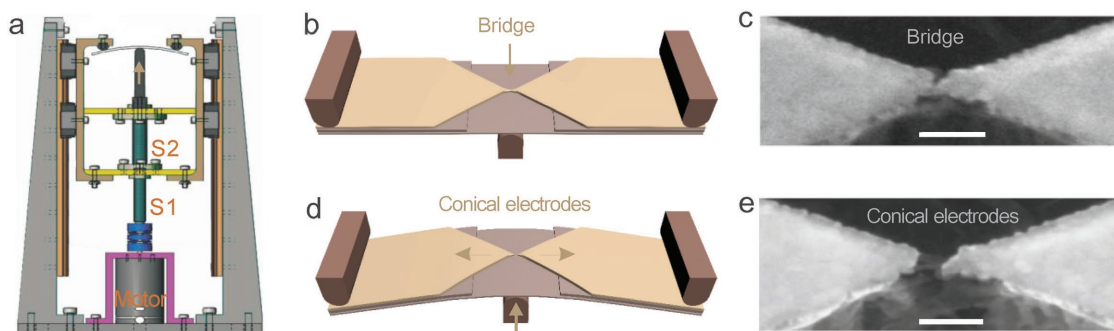
Figure 1. The fabrication of atomic-scale sharp electrodes. a) Schematic of MCBJ devices employing a differential screw as push rod. The tiny difference between the pitches of screw S1 and pitches of screw S2 allows precise control of bending of the substrate. b) Schematic of the suspended nanowire prefabricated on the substrate. c) SEM image of the suspended nanowire with a double-cone-shaped constriction in the middle as the substrate is completely relaxed. Scale bar: 10 nm. d) Schematic of the generation of atomic-scale sharp electrodes by slow bending the substrate. e) SEM image of atomic-scale sharp electrodes after the break of nanowire upon the bending of substrate. Scale bar: 10 nm.
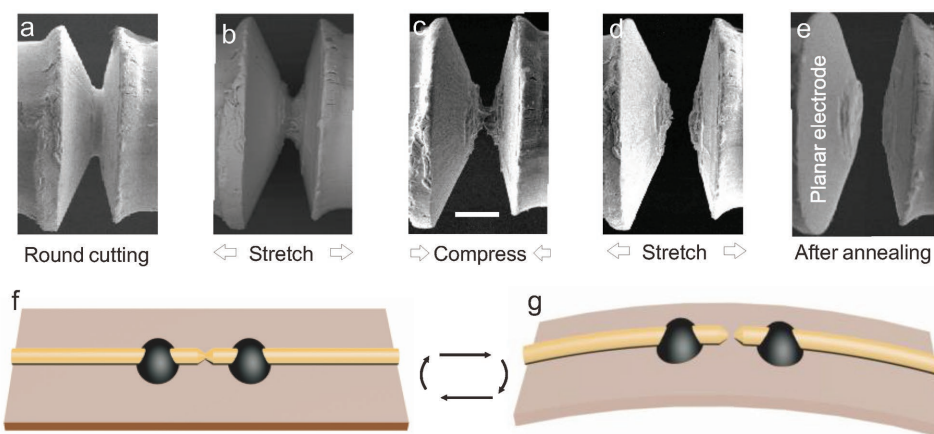
Figure 2. The fabrication of atomic-scale planar electrodes. a) A notch was made in the middle of microwire. b) The microwire was stretched to obtain two separated microelectrodes. c) The two microelectrodes collide with each other and the sharp tips on the electrodes surface were truncated as the two electrodes were compressed. Scale bar: 10 µm. d) The two electrodes can be separated once more by bending the substrate. e) SEM image of the atomic-scale planar electrodes after dozens of break–reconnect processes and one annealing process. f) Schematic of fixing the microwire onto the substrate with a notch in the middle. g) Schematic of the break of the microwire by bending the substrate.

down by bending the substrate to obtain two separated electrodes (Figure 2b). The gap size between electrodes can be reduced and even the two electrodes can be reconnected once more when the substrate is relaxed (Figure 2c). This break–reconnect process can be repeated hundreds of times for the manually fabricated samples due to the big fracture surface. The tips on the electrodes surface become blunt after several break–reconnect processes (Figure 2d). An annealing process was further performed at 300 °C for 2 h. By this annealing process, the surface of the two quasi plane-type electrodes was further smoothed due to the migration of metal atoms driven by the thermal excitation energy at the high temperature.[39] In this way, a pair of atomic-planar electrodes was obtained as shown in Figure 2e. More detailed information regarding the chip fabrication processes for two types of electrodes can be found in Figures S3–S7 in the Supporting Information, and the enlarged scanning electron microscope (SEM) picture can be found in Figures S4 and S7 (Supporting Information). The gap size between the planar electrodes can be kept constant with subangstrom accuracy over several hours (Figure S8, Supporting Information).

3. Raman Scattering Modulated by Atomic Geometries of the Electrodes

We subsequently examined the atomic-scale geometries of electrodes employing Raman scattering spectroscopy, since it is sensitive to the electrodes' atomic-scale geometry.[14,28,29,44,45] **Figure 3**a shows the schematic of Raman scattering measurement system. The incident laser was focused onto the molecular junction via a lens from the top of the MCBJ chip and the scattered light was collected directed to the spectrometer with the same lens. Figure 3b,c shows the typical surface-enhanced Raman spectroscopy (SERS) spectra obtained from the nanogap area after self-assembling of diaminobenzene (BDA) onto the electrodes surface. We found that the SERS intensity decreased when the gap size was increased from 1 to 6 nm for both types of electrodes. It is noteworthy that the Raman intensity with

planar electrodes drops faster than the one with conical electrodes, which can be clearly observed from the Raman intensity at 1568 cm^{-1} (assigned to benzene ring vibration modes).

Figure 3d–i shows the distribution of the simulated electric field dependent on the gap sizes for two types of electrodes. This simulation demonstrates that the electric field is considerably reduced when the gap size is increased from 1 to 6 nm for both types of electrodes. Meanwhile, we note that the electric field between cone-shaped electrodes is approximately one order of magnitude larger than the one between the plane-shaped electrodes with the same separation, while its field decays faster, i.e., the electric field with planar electrodes decreases faster than the one with conical electrodes which is coherent with the experimental observation (Figures S9–S11, Supporting Information). The consistency in simulated field strength and measured Raman intensity indicates that the sensitivity of Raman scattering can be really modulated via local atomic-scale geometries of the electrodes. These simulation data also indicate that SERS signals of molecules trapped within the two electrode apexes are many orders of magnitude stronger than those on flat surfaces. In other words, the detected Raman signal contributed from the molecules trapped in the gap is predominant.

4. Conductance Dependent on Electrodes' Geometries

The conductance traces of BDA molecular junction recorded for two types of electrodes during the separation processes are shown in **Figure 4**a. During the initial stage of stretching the nanowire, the conductance decreased in a stepwise fashion, with each step occurring preferentially at an integer multiple of conductance quantum $G_0 = 2e^2/h$ (h is Planck's constant and e is the electron charge). Additional plateaus at values below 1 G_0 were typically observed for both cone-shaped and plane-shaped electrodes after self-assembling of molecules onto the electrode surface. Approximately 40% conductance traces show this stepwise feature after the break of metal wire. These additional

**ADVANCED
SCIENCE NEWS**
www.advancedsciencenews.com

NANO · MICRO
small
www.small-journal.com
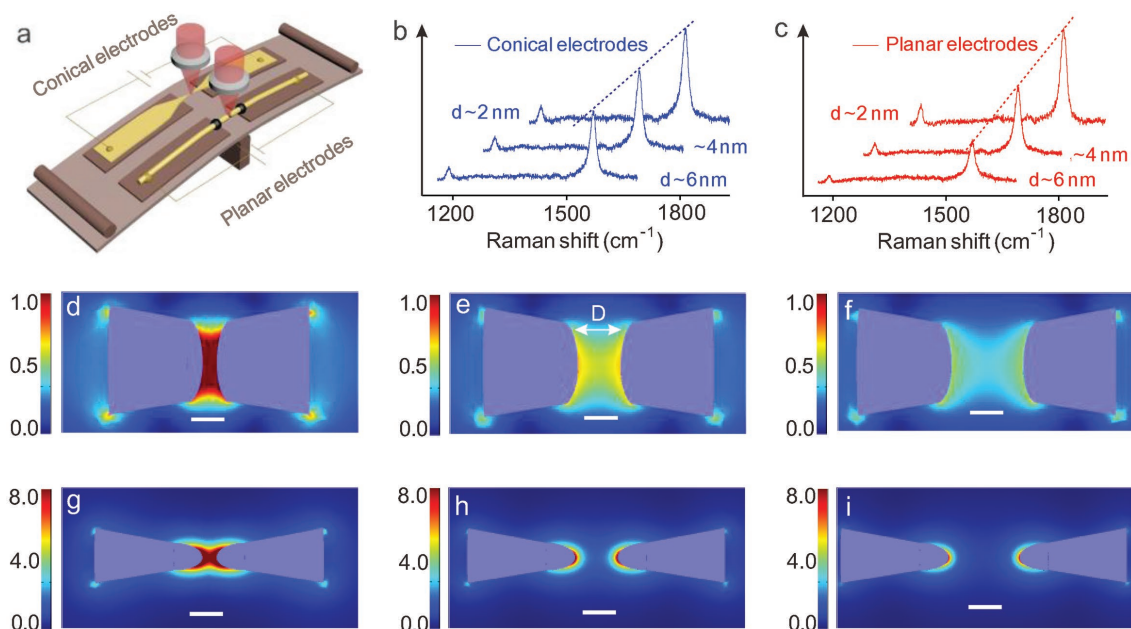
Figure 3. Modulation of Raman scattering with two types of electrodes. a) Schematic of the experimental setup combined Raman spectrometer with MCBJ. b) Raman spectroscopy of diaminobenzene upon different gap size employing the conical electrodes. c) Raman spectroscopy employing planar electrodes. Laser: 632.8 nm. The Raman intensity (e.g., @ 1568 cm^{-1} linked by the dashed line) decreases as the gap size increases for both the conical electrodes and the planar electrodes, but the decreased speeds are different for two types of electrodes. d–f) Distribution of the electric field with gap sizes of 1, 3, and 5 nm between plane-shaped electrodes. Unit: 10^7 V mm^{-1}. g–i) Distribution of the electric field between cone-shaped electrodes with gap sizes of 1, 3, and 5 nm. Unit: 10^7 V mm^{-1}. Scale bare: 2 nm.
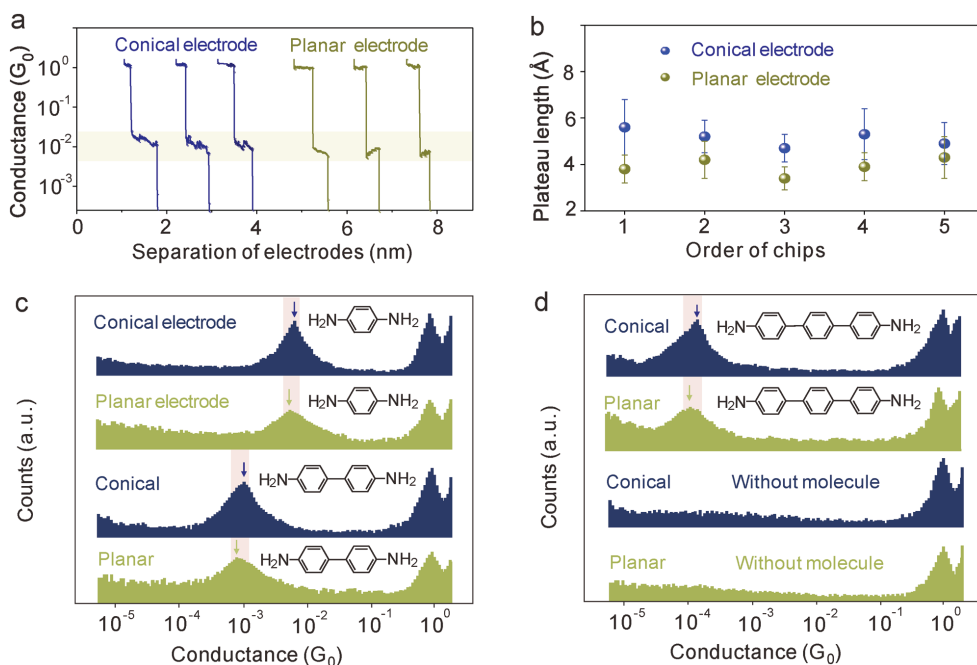
Figure 4. Effect of the electrode geometry on the conductance of single-molecule junctions. a) Conductance traces during the separation of two types of molecular junctions. The blue curves were recorded with the cone-shaped electrodes and the yellow curves were recorded with the plane-shaped electrodes. The shade area marks the conductance plateau area during the separation of molecular junctions. b) The statistical data of the conductance plateau length for two types of molecular junctions. c,d) Conductance histograms with three kinds of molecules sandwiched between two types of electrodes. Typical peaks indicated by the arrows were observed for all the six types of molecular junctions. The histogram peaks broaden and shift to lower values as the cone-shaped electrodes are replaced by plane-shaped electrodes, independent of the studied molecules. On the contrary, no typical peaks were observed when the molecules were absent (bottom panel of part (d)).

ADVANCED
SCIENCE NEWS
www.advancedsciencenews.com

NANO MICRO
small
www.small-journal.com

plateaus indicate the state that the electrodes are bridged with the molecules, and the last plateau in the step-like conductance traces indicates that the single molecule was bridging the two electrodes. On closer examination of these additional plateaus, a number of interesting features are apparent: (1) the conductance plateau for cone–molecule–cone (CMC) junctions is higher than that for the plane–molecule–plane (PMP) junctions; (2) the length of the conductance plateaus for the CMC junctions is longer than that for the PMP junctions; and (3) the plateaus for CMC junctions typically show a zigzag decreasing behavior during the electrode separation process. In contrast, the plateaus for the PMP junctions show a monotonic increasing behavior during the separation of electrodes. These distinctions for two different types of electrodes will be discussed further in Section 5.

Figure 4b shows statistical length of the conductance plateau during the stretching process with two types of electrodes (the blue curves are for cone–molecule–cone junctions, and the yellow curves are for plane–molecule–plane junctions). From Figure 4b, it can be found that the conductance plateaus obtained from cone-shaped electrodes are longer than the one obtained from plane-shaped electrodes. Notably, the molecule–electrode bond (Au−N) is weaker than the inner atomic bonds (Au−Au) of the electrode.[46,47] Thus, during the stretching process, the Au−N bond always breaks prior to the Au−Au bond. In this sense, the electrode surface geometry is insensitive to the break of the molecular junctions. In other words, the local geometry of the electrode can be generally maintained during the molecular break and reconnection process.

To verify our observations mentioned above, we investigated a series of molecules with amine linker groups using statistical methods. Figure 4c,d shows the conductance histograms of six types of molecule junctions employing both the cone-shaped and plane-shaped electrodes. Each histogram is created from ≈500 conductance traces. Two features can be observed if we take a close look at these histograms. First, regardless of the type of molecules, the peak positions in the histogram shift to lower values when the cone-shaped electrodes is used, i.e., the probable conductance with the plane-shaped electrodes is ≈50% lower compared to those with the cone-shaped electrodes. This observation deviates from general expectation. One can assume that the plane-shaped electrodes providing a relatively large surface enable the formation of both the metal–molecule–metal junction and the metal–space–metal junction in parallel simultaneously. When the distance between the bare metal electrodes is quite small in the metal–space–metal junction, the tunneling current passed through the free space will be non-negligible which will lead to an increase in the measured conductance. Therefore, the general expected conductance of the PMP junctions should be higher than that of the CMC junctions. Second, the peaks in the histogram with cone-shaped electrodes are sharper than those with plane-shaped electrodes, especially for the right shoulders of the peaks. That is to say, CMC junctions show steadier electrical behavior compared with PMP junctions. We attribute this feature to the following factors: (1) background noise is suppressed when the cone-shaped electrodes are employed. It can be observed that the background counts (village and neighbor to the main peak) in the conductance histogram are greatly reduced when cone-shaped

electrodes are used, which result in an improved noise-to-signal ratio; (2) the plane-shaped electrodes have a certain probability of sandwiching several molecules with different configurations before the last break of the junctions which is more unlikely for the cone-shaped electrodes, resulting in the broadening of the right shoulders of the histogram peaks.

5. Mechanism Discussion Based on DFT Calculation

In order to clarify the mechanism for the conductance modulation by electrodes' geometry, we performed calculations based on density functional theory. **Figure 5**a,b shows the models for the geometric optimizations and stretching simulation with the atomic-scale sharp and the atomic-scale planar electrodes, respectively. We choose 2–4 layers of Au atoms which are close to the functional molecules to construct extended molecules to perform a stretching process as outlined by the dashed line. After the geometry optimization, it is found that the dihedral angle, i.e., the angle between the terminal −NH$_2$ plane and the neighboring benzene plane, is ≈180° for the plane-type connections which are the typical geometries of amine groups with sp^2 hybridizations. However, this dihedral angle is only ≈130° for cone-type connections, which indicates that the sp^3 hybridizations have been induced by the cone-shaped electrodes from the sp^2 hybridizations of terminal amine groups. More detailed information can be found in the Supporting Information and is shown in Figure S12 (Supporting Information).

Figure 5c shows the geometric evolutions of the 1,4-diaminobenzene molecular junctions with cone-shaped electrodes. The simulations show that two terminal −NH$_2$ groups adsorb onto the second edge Au atoms of the two cone-shaped electrodes after the Au−Au contact breaks at $X = 1.69$ nm (Figure 5c, state 1). The lower amine group of the molecule shifted from the second edge Au atom to the top Au atom at $X = 1.91$ nm (state 2). We found that a stretching force of ≈0.24 nN is needed for this shift of the terminal amine group. When the space between the electrodes is further increased to ≈2.13 nm, two interesting processes occur. In the first case, the upper amine terminal shifts straightly from the second edge Au atom and adsorbs onto the top Au atom of the electrode (state 3). Upon further stretching of the electrodes, the molecule will break from the gold atom at $X = 2.40$ nm with a stretching force of 0.32 nN (state 4). When the electrodes are separated gradually with slow speed, another configurational change will occur, as shown in Figure S13 (Supporting Information).

Figure 5d show the simulated conductance traces for the CMC-type junctions. Segments 1–4 of the curves correspond to the configurations (states 1–4) as shown in Figure 5c. It shows that the conductance trace of the CMC-type junction exhibits a zigzag feature, which corresponds to the process of the terminal amine group shifting from the edge Au atom to the top Au atom of the electrode. The most probable conductance value of 1, 4-diaminobenzene with the CMC junction is 7.0×10^{-3} G_0 (Figure S14, Supporting Information).

In contrast, the molecule is compressed in the PMP junction with an initial gap size of ≈1.48 nm (Figure 5e, state A). The

ADVANCED
SCIENCE NEWS
www.advancedsciencenews.com

NANO MICRO
small
www.small-journal.com
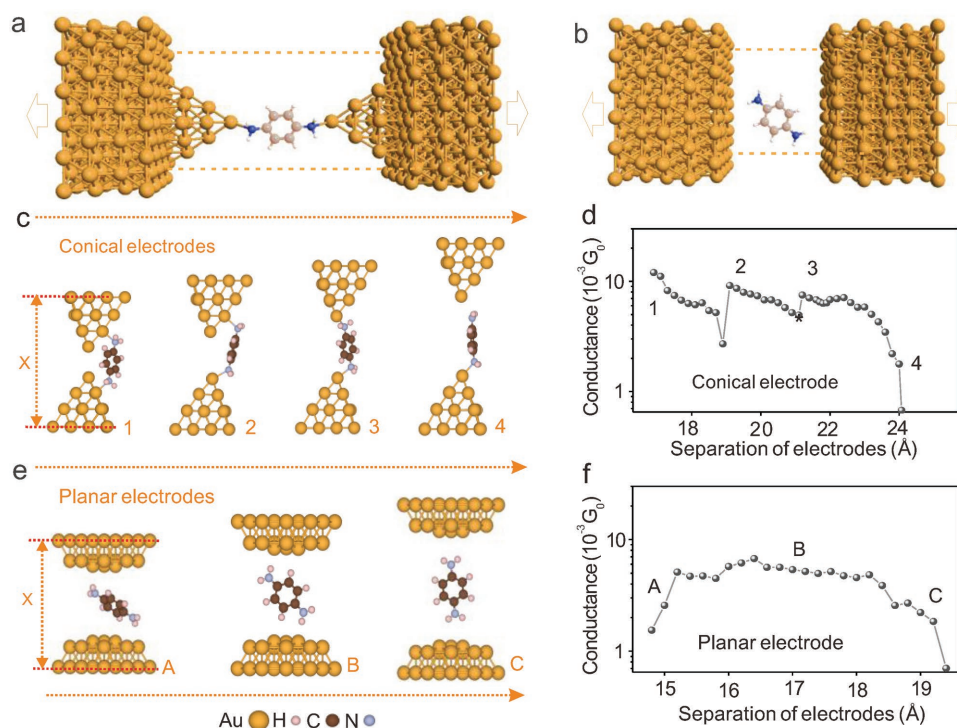
Figure 5. The simulation of elongation processes for 1,4-diaminobenzene molecular junctions. a) The models for the stretching simulation with atomic-scale sharp electrodes and b) atomic-scale planar electrodes. c) The stretching processes and corresponding conductance trace d) of the molecular junctions with atomic-scale sharp electrodes. The electrode spacing (X) is defined as the distance between the fixed Au atoms of the two electrodes. e) The geometric evolution of the molecular junction and corresponding conductance trace f) upon stretching with atomic-scale planar electrodes.

molecular plane becomes perpendicular to the electrode surface when the electrode separation is increased to $X = 1.60$ nm (state B). The molecule will rotate gradually until the N—N axis is approximately perpendicular to the electrode plane at $X = 1.88$ nm, and the junction completely breaks at $X = 1.92$ nm (state C) with a break force of ≈0.13 nN. No obvious zigzag-type conductance trace was observed in the PMP junction as shown in Figure 5f. The calculated conductance increases during the initial stretching process, which is opposite to the feature with the CMC molecular junctions. This feature is attributed to the fact that the molecule can be initially compressed between the plane-type electrodes with big surface area, resulting in a tilted molecule that rarely appears in the CMC junctions. The

separation of the electrodes leads to a release of the molecules, i.e., the tilted angle is reduced and becomes perpendicular to the electrode surface. In PMP junction, the molecule is connected with electrodes via the terminal hydrogen atoms (chemical bond was not formed); thus, the coupling strength between molecule and electrodes is weaker than the one in CMC junction, see further discussion in the following section. The probable conductance value of the PMP molecular junctions is 5.0×10^{-3} G_0 (Figure S14, Supporting Information), which is smaller than the one of CMC junctions.

The measured conductance employing two types of electrodes together with the calculated data is summarized in **Table 1**. The CMC molecular junctions always show higher conductance, not

Table 1. Conductance of molecular junctions with different electrode geometries.

Molecules	Measured junction conductance[a] [G_0]			Calculated junction conductance [G_0]		
	CMC	CMP[b]	PMP	CMC	CMP	PMP
H_2N-⬡-NH_2	8.5×10^{-3}	6.4×10^{-3}	5.8×10^{-3}	7.0×10^{-3}	6.1×10^{-3}	5.0×10^{-3}
H_2N-⬡-⬡-NH_2	1.2×10^{-3}	1.1×10^{-3}	8.0×10^{-4}	1.0×10^{-3}	8.6×10^{-4}	6.8×10^{-4}
H_2N-⬡-⬡-⬡-NH_2	1.5×10^{-4}	1.3×10^{-4}	1.1×10^{-4}	1.4×10^{-4}	1.1×10^{-4}	0.9×10^{-4}
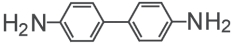
[a]The bias voltage for the conductance measurement is 13 mV; [b]The data were taken from ref. [52] and measured by scanning tunneling microscopy. Molecules: (1) 1,4-diaminobenzene; (2): 4,4′-diaminobiphenyl; and (3): 4,4′-diaminotriphenyl.

**ADVANCED
SCIENCE NEWS**

www.advancedsciencenews.com

NANO | MICRO

small

www.small-journal.com
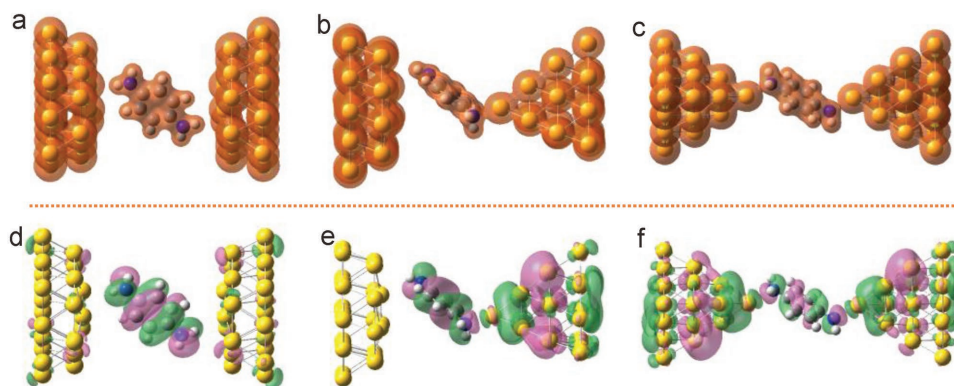
Figure 6. Spatial distributions of Fermi potential surfaces and highest occupied molecular orbitals. The spatial distributions of a–c) the Fermi potential surfaces and d–f) the highest occupied molecular orbitals for the three different types of diaminobenzene junctions with cone-shaped electrodes and plane-shaped electrodes, respectively.

only for the diaminobenzene molecular junctions but also for the diaminobiphenyl and diaminotriphenyl junctions. The conductance of the CMC molecular junctions is ≈1.2 times larger than the conductance of the CMP molecular junctions and is ≈1.5 times larger than the conductance of the PMP molecular junctions. Here, we assume that the configuration of molecular junctions generated by scanning tunneling microscopy, in which a sharp tip and a smooth substrate are used to form the molecular bridge, can be look as CMP configuration.[52]

To further understand the conductance performance in different types of molecular junctions, we present the spatial distribution of the Fermi potential surfaces (FPS) at equilibrium distance (**Figure 6**a–c). The FPS of the three types of molecular systems shows remarkable differences. A gap exists between the molecule and electrode in the FPS for the plane-shaped electrode (Figure 6a). This gap indicates that there is a potential barrier between the molecule and the plane-shaped electrode for the electron transport. In contrast, the FPS of the molecule overlaps the cone-shaped electrode due to the sp^3 hybridization of the terminal amine groups induced by the Au atoms arranged in a cone shape (Figures 6b,c), strengthening the coupling between the molecule and the electrode. Based on the one-dimension transmission combined with the three-dimension correction approximation (OTCTCA) method and quantum mechanics theory,[48] the transmission probability should be reduced for PMP junctions due to the potential barriers between the molecule and electrodes.

Figure 6d–f presents the spatial distributions of the highest occupied molecular orbitals (HOMOs) of diaminobenzene molecular junctions with the three types of connections. The HOMO is only located on the two plane-shaped electrodes for the PMP junction (Figure 6d). In contrast, the HOMO of the CMC junction is delocalized all over the molecular junction (Figure 6e,f). That is, the HOMO strengthens the coupling between the molecule and the cone-shaped electrodes, which consequently results in a proportion of sp^3 hybridizations at terminal amine groups from pure sp^2 hybridizations and further eliminates the gaps between the molecule and the electrode. As a rule of thumb, the weak coupling will lead to a poor conductance; thus, it is reasonable to observe low conductance in molecular junctions employing plane-shaped electrodes.

Now, we can reach to the conclusion that the stability of molecular device can be greatly improved when cone-shaped electrodes are used based on the observations: (1) the molecule–electrode coupling is significantly enhanced with the conical electrodes; (2) the force to break junction is increased as the conical electrodes are employed; (3) the length of the conductance plateaus employing cone-shaped electrodes is longer than the one employing plane-shaped electrodes; and (4) the noise-to-signal ratio is improved with cone-shaped electrodes. We believe that our conclusion should be universally suitable for the molecules with weak linker groups (the bond force between the molecule and electrodes is weaker than the internal Au—Au bond of the electrodes). However, for those molecules with strong bonds, e.g., sulfur-anchoring group, a different result may occur due to the different coupling mechanism. Our initial calculation shows that the molecular junctions employing planar electrodes are more stable than the one with conical electrodes if Au—S bonds are used to link the molecules, which is opposite to the conclusion made in this paper. Thus, further systemically investigations are deserved to clarify the effect of the electrode geometry for the various molecules.

6. Conclusion

To conclude, both atomic-scale sharp and atomic-scale planar electrodes have been fabricated: the former is fabricated by precisely stretching a nanowire while the latter is generated by the mechanically collision of atoms on the electrodes' tip surface. Moreover, the gap size between electrodes can be precisely controlled with subangstrom accuracy after the formation of target electrodes. Combining these two achievements, we can modulate electron transport as well as localized surface plasmon in the molecular junctions. It is amazing to observe that the conductance of single-molecule junctions employing atomic-scale sharp electrodes is ≈50% higher than the one employing atomic-scale planar electrodes for those molecules with amine bonding groups. The underneath mechanism for this observation was revealed by ab initio calculations, that is, atomic-scale sharp electrodes induces sp^3 hybridizations of terminal amine groups which strengthens the coupling between

ADVANCED
SCIENCE NEWS
www.advancedsciencenews.com

NANO MICRO
small
www.small-journal.com

molecule and electrodes. Meanwhile, it is confirmed that the stability of molecule junction can be improved by atomic-planar electrodes, but the sensitivity of Raman scattering can only be improved by atomic-scale planar electrodes. Our results not only contribute to improving the stability of single molecular junctions as well as to controlling electron transport through molecular devices, but also provide a potential platform to study the interaction between electron transport and Raman scattering in the future.

7. Experimental Section

Raman Spectroscopy Measurements: The Raman spectroscopic measurements were made using a Jobin Yvon system and the spectra were collected in a backscattering geometry with a confocal Raman microscope equipped with 100× objective. Si_3N_4 was employed as the insulation layer instead of polyimide for Raman scattering characterization, by which the background fluorescence signal from the insulation layer was reduced. It took 10 min for the molecules to assemble followed by a rinsing process. The Raman scattering was measured in a dry condition, the same as the conductance measurement. Before carrying out a detailed SERS study on the molecular junctions, the SERS activity of different parts of the electrodes' surface, such as the edge and gap, was first analyzed. The SERS measurement was started with a set gap size of 1 nm and ended with a gap size of 6 nm. As the gap size was changed, the optics was adjusted synchronously to ensure that the SERS intensity change was solely due to the gap change.

Electric Field Simulations: Simulations were performed to present the distribution of the electric field using the finite-element method with the COMSOL Multiphysics software. The total simulation region was set to 15 nm × 15 nm × 40 nm in air. The electrodes model was built by combining a circular truncated cone with an ellipsoid. A plane wave (wavelength 632.8 nm) was impinged on the gold electrodes with a polarization parallel to the electrode–electrode direction. The refractive index ($n = 0.27732$) and the extinction coefficient ($k = 2.9278$) of gold were used for the simulations.[49] The averaged electric field strength was detected by a surface probe set on the ellipsoid surface as the nanogap size was changed from 1 to 6 nm with a step size of 0.5 nm. The simulation was also performed using an atomistic electrodynamics model, and the coherent results were obtained (see Figures S10 and S11 in the Supporting Information).

Conductance Measurements: The self-assembly of the molecules on the gold nanowire surface was performed in a freshly prepared solution (1×10^{-3} M) in 1,2,4-trichlorobenzene (99% Aldrich). After a self-assembly period of 10 min on the Au surface, the sample was rinsed with ethanol and dried under a nitrogen stream. Subsequently, the samples were mounted into the MCBJ setup in a vacuum chamber for conductance measurements. Please note that, for plane-shaped electrodes, the self-assembly of the molecules was performed after the annealing process of the microwire, and the distance between electrodes was set to be ≈10 nm. The length of conductance plateau was counted based on the conductance traces as shown in Figure 4a. The start point was chosen at the point as a conductance plateau appears just after a jump at G_0 (it corresponds to the separation of gold–gold), and the end point was chosen just before a new big jump appeared (it corresponds the break of molecular junction). The error bar was determined based on the data collected from ten junctions with one chip.

DFT Calculations: The geometric optimizations of these molecular junctions were performed at the B3LYP level with the Lanl2DZ basis set in the Gaussian 03 packages.[50] The conductance evolution in the elongation process was calculated employing the OTCTCA method.[48] In the simulation, both the molecules and Au atom neighbors of the functional molecules were relaxed by performing geometric optimizations. However, the outer-side Au layers were fixed in order to execute the elongation successively as reported in the previous work.[48,51]

[1] M. L. Perrin, E. Burzurí, H. S. J. van der Zant, *Chem. Soc. Rev.* **2015**, *44*, 902.

[2] D. Xiang, X. L. Wang, C. C. Jia, T. Lee, X. F. Guo, *Chem. Rev.* **2016**, *116*, 4318.

[3] L. Sun, Y. A. Diaz-Fernandez, T. A. Gschneidtner, F. Westerlund, S. Lara-Avila, K. Moth-Poulsen, *Chem. Soc. Rev.* **2014**, *43*, 7378.

[4] K. Moth-Poulsen, *Handbook of Single-Molecule Electronics*, CRC Press, Boca Raton, FL **2016**.

[5] S. J. van der Molen, R. Naaman, E. Scheer, J. B. Neaton, A. Nitzan, D. Natelson, N. J. Tao, H. van der Zant, M. Mayor, M. Ruben, M. Reed, M. Calame, *Nat. Nanotechnol.* **2013**, *8*, 622.

[6] C. C. B. Bufon, J. D. A. Espinoza, D. J. Thurmer, M. Bauer, C. Deneke, U. Zschieschang, H. Klauk, O. G. Schmidt, *Nano Lett.* **2011**, *11*, 3727.

[7] K. C. Liao, C. M. Bowers, H. J. Yoon, G. M. Whitesides, *J. Am. Chem. Soc.* **2015**, *137*, 3852.

[8] C. Jia, A. Migliore, N. Xin, S. Huang, J. Wang, Q. Yang, S. Wang, H. Chen, D. Wang, B. Feng, Z. Liu, G. Zhang, D.-H. Qu, H. Tian, M. A. Ratner, H. Q. Xu, A. Nitzan, X. Guo, *Science* **2016**, *352*, 1443.

[9] J. G. Kushmerick, J. Naciri, J. C. Yang, R. Shashidhar, *Nano Lett.* **2003**, *3*, 897.

[10] Y. L. Loo, D. V. Lang, J. A. Rogers, J. W. P. Hsu, *Nano Lett.* **2003**, *3*, 913.

[11] J. J. Parks, A. R. Champagne, T. A. Costi, W. W. Shum, A. N. Pasupathy, E. Neuscamman, S. Flores-Torres, P. S. Cornaglia, A. A. Aligia, C. A. Balseiro, G. K. L. Chan, H. D. Abruña, D. C. Ralph, *Science* **2010**, *328*, 1370.

[12] S. Y. Sayed, J. A. Fereiro, H. J. Yan, R. L. McCreery, A. J. Bergren, *Proc. Natl. Acad. Sci. USA* **2012**, *109*, 11498.

[13] B. Sun, M. Wang, Z. C. Lou, M. J. Huang, C. L. Xu, X. H. Li, L. J. Chen, Y. H. Yu, G. L. Davis, B. Q. Xu, H. B. Yang, X. P. Li, *J. Am. Chem. Soc.* **2015**, *137*, 1556.

[14] D. R. Ward, N. J. Halas, J. W. Ciszek, J. M. Tour, Y. Wu, P. Nordlander, D. Natelson, *Nano Lett.* **2008**, *8*, 919.

[15] A. P. Bonifas, R. L. McCreery, *Nano Lett.* **2011**, *11*, 4725.

[16] P. Pang, B. A. Ashcroft, W. S. Song, P. M. Zhang, S. Biswas, Q. Qing, J. L. Yang, R. J. Nemanich, J. W. Bai, J. T. Smith, K. Reuter, V. S. K. Balagurusamy, Y. Astier, G. Stolovitzky, S. Lindsay, *ACS Nano* **2014**, *8*, 11994.

[17] T. Shamai, A. Ophir, Y. Selzer, *Appl. Phys. Lett.* **2007**, *91*, 102108.

[18] A. Vezzoli, R. J. Brooke, N. Ferri, S. J. Higgins, W. Schwarzacher, R. J. Nichols, *Nano Lett.* **2017**, *17*, 1109.

[19] A. K. Ismael, K. Wang, A. Vezzoli, M. K. Al-Khaykanee, H. E. Gallagher, I. M. Grace, C. J. Lambert, B. Xu, R. J. Nichols, S. J. Higgins, *Angew. Chem., Int. Ed.* **2017**, *56*, 15378; *Angew. Chem.* **2017**, *129*, 15580.

[20] A. Vezzoli, R. J. Brooke, S. J. Higgins, W. Schwarzacher, R. J. Nichols, *Nano Lett.* **2017**, *17*, 6702.

[21] C. Huang, A. V. Rudnev, W. Hong, T. Wandlowski, *Chem. Soc. Rev.* **2015**, *44*, 889.

[22] D. L. Bao, R. Liu, J. C. Leng, X. Zuo, Y. Jiao, Z. L. Li, C. K. Wang, *Phys. Lett. A* **2014**, *378*, 1290.

[23] X. X. Fu, R. Q. Zhang, G. P. Zhang, Z. L. Li, *Sci. Rep.* **2015**, *4*, 6357.

[24] G. P. Zhang, G. C. Hu, Y. Song, Z. L. Li, C. K. Wang, *J. Phys. Chem. C* **2012**, *116*, 22009.

[25] P. Moreno-García, M. Gulcur, D. Z. Manrique, T. Pope, W. Hong, V. Kaliginedi, C. Huang, A. S. Batsanov, M. R. Bryce, C. Lambert, *J. Am. Chem. Soc.* **2013**, *135*, 12228.

[26] L. Grüter, M. T. González, R. Huber, M. Calame, C. Schönenberger, *Small* **2005**, *1*, 1067.

[27] S. Kaneko, D. Murai, S. Marqués-González, H. Nakamura, Y. Komoto, S. Fujii, T. Nishino, K. Ikeda, K. Tsukagoshi, M. Kiguchi, *J. Am. Chem. Soc.* **2016**, *138*, 1294.

[28] T. Konishi, M. Kiguchi, M. Takase, F. Nagasawa, H. Nabika, K. Ikeda, K. Uosaki, K. Ueno, H. Misawa, K. Murakoshi, *J. Am. Chem. Soc.* **2013**, *135*, 1009.

[29] Z. Liu, S.-Y. Ding, Z.-B. Chen, X. Wang, J.-H. Tian, J. R. Anema, X.-S. Zhou, D.-Y. Wu, B.-W. Mao, X. Xu, B. Ren, Z.-Q. Tian, *Nat. Commun.* **2011**, *2*, 305.

[30] S. M. Wu, M. T. González, R. Huber, S. Grunder, M. Mayor, C. Schönenberger, M. Calame, *Nat. Nanotechnol.* **2008**, *3*, 569.

[31] S. Ballmann, R. Härtle, P. B. Coto, M. Elbing, M. Mayor, M. R. Bryce, M. Thoss, H. B. Weber, *Phys. Rev. Lett.* **2012**, *109*, 56801.

[32] M. A. Karimi, S. G. Bahoosh, M. Herz, R. Hayakawa, F. Pauly, E. Scheer, *Nano Lett.* **2016**, *16*, 1803.

[33] C. Y. Liu, S. Kaneko, Y. Komoto, S. Fujii, M. Kiguchi, *Appl. Phys. Lett.* **2015**, *106*, 103103.

[34] D. Z. Manrique, C. Huang, M. Baghernejad, X. T. Zhao, O. A. Al-Owaedi, H. Sadeghi, V. Kaliginedi, W. J. Hong, M. Gulcur, T. Wandlowski, M. R. Bryce, C. J. Lambert, *Nat. Commun.* **2015**, *6*, 6389.

[35] M. L. Perrin, C. J. O. Verzijl, C. A. Martin, A. J. Shaikh, R. Eelkema, J. H. van Esch, J. M. van Ruitenbeek, J. M. Thijssen, H. S. J. van der Zant, D. Duli , *Nat. Nanotechnol.* **2013**, *8*, 282.

[36] J. Ponce, C. R. Arroyo, S. Tatay, R. Frisenda, P. Gaviña, D. Aravena, E. Ruiz, H. S. J. van der Zant, E. Coronado, *J. Am. Chem. Soc.* **2014**, *136*, 8314.

[37] C. Schirm, M. Matt, F. Pauly, J. C. Cuevas, P. Nielaba, E. Scheer, *Nat. Nanotechnol.* **2013**, *8*, 645.

[38] J. H. Tian, B. Liu, X. L. Li, Z. L. Yang, B. Ren, S. T. Wu, N. J. Tao, Z. Q. Tian, *J. Am. Chem. Soc.* **2006**, *128*, 14748.

[39] M. Tsutsui, T. Morikawa, Y. H. He, A. Arima, M. Taniguchi, *Sci. Rep.* **2015**, *5*, 11519.

[40] S. Wagner, F. Kisslinger, S. Ballmann, F. Schramm, R. Chandrasekar, T. Bodenstein, O. Fuhr, D. Secker, K. Fink, M. Ruben, H. B. Weber, *Nat. Nanotechnol.* **2013**, *8*, 575.

[41] T. Yelin, R. Vardimon, N. Kuritz, R. Korytar, A. Bagrets, F. Evers, L. Kronik, O. Tal, *Nano Lett.* **2013**, *13*, 1956.

[42] D. Xiang, H. Jeong, D. Kim, T. Lee, Y. J. Cheng, Q. L. Wang, D. Mayer, *Nano Lett.* **2013**, *13*, 2809.

[43] Q. Wang, R. Liu, D. Xiang, M. Sun, Z. Zhao, L. Sun, T. Mei, P. Wu, H. Liu, X. Guo, Z. L. Li, T. Lee, *ACS Nano* **2016**, *10*, 9695.

[44] T. Shamai, Y. Selzer, *Chem. Soc. Rev.* **2011**, *40*, 2293.

[45] X. Wu, E. Thrall, H. Liu, M. Steigerwald, L. Brus, *J. Phys. Chem. C* **2010**, *114*, 12896.

[46] Y. Kim, T. J. Hellmuth, M. Bürkle, F. Pauly, E. Scheer, *ACS Nano* **2011**, *5*, 4104.

[47] S. Y. Quek, H. J. Choi, S. G. Louie, J. B. Neaton, *Nano Lett.* **2009**, *9*, 3949.

[48] R. Liu, C. K. Wang, Z. L. Li, *Sci. Rep.* **2016**, *6*, 21946.

[49] P. B. Johnson, R. W. Christy, *Phys. Rev. B* **1972**, *6*, 4370.

[50] M. J. Frisch, G. W. Trucks, H. B. Schlegel, G. E. Scuseria, M. A. Robb, J. R. Cheeseman, G. Scalmani, V. Barone, B. Mennucci, G. A. Petersson, H. Nakatsuji, M. Caricato, X. Li, H. P. Hratchian, A. F. Izmaylov, J. Bloino, G. Zheng, J. L. Sonnenberg, M. Hada, M. Ehara, K. Toyota, R. Fukuda, J. Hasegawa, M. Ishida, T. Nakajima, Y. Honda, O. Kitao, H. Nakai, T. Vreven, J. A. MontgomeryJr., J. E. Peralta, F. Ogliaro, M. J. Bearpark, J. Heyd, E. N. Brothers, K. N. Kudin, V. N. Staroverov, R. Kobayashi, J. Normand, K. Raghavachari, A. P. Rendell, J. C. Burant, S. S. Iyengar, J. Tomasi, M. Cossi, N. Rega, N. J. Millam, M. Klene, J. E. Knox, J. B. Cross, V. Bakken, C. Adamo, J. Jaramillo, R. Gomperts, R. E. Stratmann, O. Yazyev, A. J. Austin, R. Cammi, C. Pomelli, J. W. Ochterski, R. L. Martin, K. Morokuma, V. G. Zakrzewski, G. A. Voth, P. Salvador, J. J. Dannenberg, S. Dapprich, A. D. Daniels, Ö. Farkas, J. B. Foresman, J. V. Ortiz, J. Cioslowski, D. J. Fox, *Gaussian 03*, Gaussian, Inc., Wallingford, CT, USA **2003**.

[51] R. Liu, D. L. Bao, Y. Jiao, L. W. Wan, Z. L. Li, C. K. Wang, *Acta Phys. Sin.* **2014**, *63*, 68501.

[52] L. Venkataraman, J. E. Klare, C. Nuckolls, M. S. Hybertsen, M. L. Steigerwald, *Nature* **2006**, *442*, 904.